Materials Advances

ROYAL SOCIETY OF CHEMISTRY

PAPER

View Article Online
View Journal | View Issue

Check for updates

Cite this: *Mater. Adv.*, 2023, 4, 954

In situ synthesis and properties of $Ag/Ag_{10}Si_4O_{13}$/GO photocatalysts with synergistic effect of plasma Resonance and Schottky junction†

Cuixia Li, *[ab] Ruilin Zhang,[a] Youyou Zhang,[a] Haize Jin,[a] Yuhang Zhang[a] and Wensheng Li*[ab]

Received 25th June 2022,
Accepted 21st December 2022

DOI: 10.1039/d2ma00743f

rsc.li/materials-advances

Ongoing studies on photocatalysts based on the response of the overall band spectrum of visible light to clean water resources have received significant attention. This study focuses on the synergistic effect of plasma resonance and Schottky junction of silver as a promoter in $Ag_{10}Si_4O_{13}$/GO-based photocatalysts for improving the photocatalytic performance and stability. The nanostructured $Ag/Ag_{10}Si_4O_{13}$/GO composites were synthesized by an accurate molecular (ion) scale assembly based on the sol–gel method. The response range of visible light was extended to 660 nm, and the combined effect of the Schottky junction and internal polarization electric field of $Ag_{10}Si_4O_{13}$ showed excellent charge separation efficiency. The highly efficient non-selective degradation for cationic and anionic dyes was demonstrated under visible light, and methylene blue (20 g mL^{-1}) can be completely degraded in 15 min. The excellent cycling stability was obtained due to the inhibition of photoreduction. The novel nano-engineering strategy provided a new reference for highly active photocatalysts.

1. Introduction

The rapid development and capacity expansion of textile and printing result in the production of a large number of dyes wastewater,[1,2] which has been one of the serious routes for the generation of gray/polluted water.[3] Semiconductor photocatalytic oxidation, as a type of advanced oxidation processing with the potential to overcome energy shortage and solve environmental pollution problems, utilizes sunlight for the non-selective and efficient degradation of organic pollutants in the presence of water without secondary pollution.[4–6] Many efforts have been made in the direction of classic photocatalytic materials such as titanium dioxide (TiO_2) to improve the photocatalytic performance and improve the visible light response ability.[7–13] However, the improvement of the intrinsic properties of TiO_2 or other wide band-gap semiconductor materials by ion doping, construction of heterojunction, noble metal-modification, *etc.*, is limited. In recent years, the development of silver-based photocatalysts (Ag_2O,[14] AgBr,[15] AgI2,[16] Ag_3PO_4,[17,18] *etc.*) with small band gaps and unique electronic configurations provides a broad way to solve this problem effectively.

As a new type of silver-based photocatalysts, silver silicate ($Ag_xSi_yO_z$) photocatalysts could provide empty 5s orbital and potentially the 5p orbital to accept additional electrons due to Ag ions forming FCC cluster-like aggregates.[3] Combined with the unique electronic d^{10}–d^{10} structure and the internal polarization electric field induced by the distorted tetrahedral unit [SiO_4], $Ag_xSi_yO_z$ showed a strong charge separation rate.[19,20] As the strength of the internal electric field is determined by the number of the distorted [SiO_4] tetrahedra, $Ag_{10}Si_4O_{13}$ has attracted considerable attention.[21] Moreover, the effective unit cell of $Ag_{10}Si_4O_{13}$ is smaller than the metal, which has a greater propensity to generate photogenerated electrons from the surface to the interface for the photodecomposition of dye molecules.[22] Currently, solid-phase synthesis (SPS) has been proposed for the synthesis of $Ag_{10}Si_4O_{13}$ with excellent photocatalytic activity and has been further developed.[23–25] However, the enhancement of purity and controllable modification of the as-prepared $Ag_{10}Si_4O_{13}$ are relatively difficult due to ion diffusion in the solid state. In recent years, a high purity nanocrystalline preparation strategy based on the sol–gel process were proposed by our research group, which provided the possibility of atomic scale composition adjustment to further improve the degradation performance and stability of nano-$Ag_{10}Si_4O_{13}$.[3,26,27]

[a] School of Materials Science and Engineering, Lanzhou University of Technology, 287 Langongping Rd, Qilihe District, Lanzhou, Gansu, P. R. China. E-mail: licx2007@lut.cn, liws@lut.edu.cn

[b] State Key Laboratory of Advanced Processing and Recycling of Non-Ferrous Metals, Lanzhou University of Technology, 287 Langongping Rd, Qilihe District, Lanzhou, Gansu, P. R. China

† Electronic supplementary information (ESI) available. See DOI: https://doi.org/10.1039/d2ma00743f

Graphene, as a good conductor of photoelectrons, has been widely used to improve the performance of photocatalysts.[28,29] A high work function (4.42 eV) of graphene makes it a photoelectron acceptor from the conduction band of the photocatalysts.[30] Also, a high charge mobility and carrier separation efficiency can be obtained by composite graphene with semiconductors.[31,32] In addition, graphene oxide (GO), a derivative of graphene, possesses a large number of functional groups, which is conducive to the *in situ* growth of nanoparticles to inhibit agglomeration and fully exploit the utility of photocatalysts.[33] Furthermore, the introduction of silver nanoparticles into semiconductor materials has been shown to effectively improve the photocatalytic efficiency and enhance the stability due to the local surface plasmon resonance (LSPR).[34,35] Meanwhile, the construction of the Schottky junction between silver nanoparticles and semiconductor can synergically improve the photocatalytic performance.[36,37] Therefore, the *in situ* loading of $Ag_{10}Si_4O_{13}$ and Ag nanoparticles on the graphene oxide surface is expected to further improve the service stability of $Ag_{10}Si_4O_{13}$-based photocatalysts by the multiple effects of LSPR, Schottky junction, and internal polarization electric field.

The novelty of our work is in the synthesis of plasmonic nanostructured $Ag/Ag_{10}Si_4O_{13}/GO$ (AAG) composite photocatalytic materials based on the sol–gel method. GO was utilized as a carrier and the *in situ* growth mechanism of the AAG was revealed. The effects of the Ag nanoparticles dosages on the phase, microstructure, visible light photocatalytic performance, and cycling stability of AAG were studied in detail. In addition, the synergistic coupling mechanism of LSPR, Schottky junction, and internal polarization electric field were discussed. The proposed strategy could provide an important reference for the one-step synthesis of high performance $Ag_{10}Si_4O_{13}$-based photocatalysts.

2. Experimental details

2.1. Materials and reagents

Tetraethoxysilane (TEOS, ≥98%) and $AgNO_3$ (≥99.8%) were employed as the raw materials for $Ag_{10}Si_4O_{13}$. Citric acid (CA, ≥99.5%) was utilized as hydrolysis inhibitor and complexing agent. Methylene blue (MB, ≥98.5%) and methyl orange (MO, ≥98.5%) were the target degradants. $AgNO_3$, *tert*-butanol (TB, ≥95%) phthalic acid (PTA, ≥99%), and benzoquinone (P-BQ, ≥99%) served as scavengers for electron (e^-), hole (h^+), hydroxyl radical ($^\bullet OH$), and superoxide radical ($^\bullet O_2^-$), respectively. All the chemicals were used as received and without further purification. In all experiments, distilled water was used as a polar solvent. GO hydrosol was prepared from graphite powder using a modified Hummers' method, as shown in our previous work.[38] The XRD pattern and Raman spectrum of GO are given in the ESI.†

2.2. Preparation of AG and AGG composites

$Ag_{10}Si_4O_{13}/GO$ (AG) and AAG were synthesized by a simple one-step sol method to control the homogeneity of the nano-heterojunction from the molecular (ion) level. The specific experimental process is shown in Fig. 1. A certain amount of CA was mixed into absolute ethyl alcohol (25 mL), and 4.8 mL ethyl orthosilicate and 1.5 mL H_2O were added under magnetic agitation for 1 h to get colorless transparent silica sol. Then, an appropriate amount of GO sol was added to the above silica sol; the mass fraction of GO in $Ag_{10}Si_4O_{13}$ was 1 wt%. On this basis, the $AgNO_3$ solution was further dropped and the mass fractions of Ag were regulated on the basis of the silver–silicon ratio of $Ag_{10}Si_4O_{13}$. The mixtures were dried at 70 °C for 24 h and calcined at 400 °C for 5 h to obtain the AG and AGG samples with different mass fractions of Ag simple substance (0 wt%, 0.1 wt%, 0.5 wt%, and 1 wt%, named as 0.1AGG, 0.5AGG, and 1AGG).

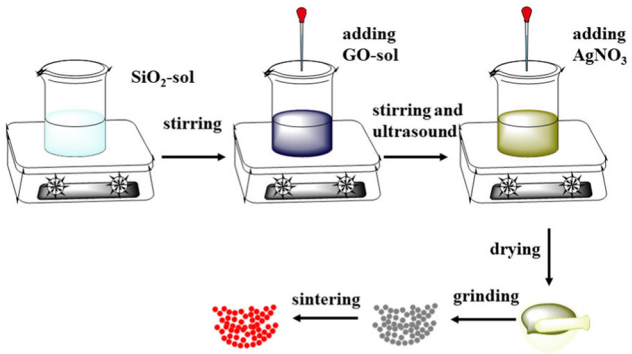

Fig. 1 Schematic illustration of the synthesis of AGG composites.

2.3. Characterization and theoretical calculations

Phase analysis was carried out by powder X-ray diffraction (XRD, D8 Advance, Bruker). The morphology of the as-prepared sample was characterized using transmission electron microscopy (TEM, Tecnai F20-G2, FEI Company). Fourier transform infrared (FTIR) spectroscopy was utilized to analyze the evolution of the chemical bond of GO, AG, and AGG (Nexus670, Nicolet). The chemical status of the sample was analyzed by X-ray photoelectron spectroscopy (XPS, PHI-5702, American physical electronics Corp.). The energy band and adsorption edge were evaluated using a UV-vis spectrophotometer (U-3900H, Hitachi). The zeta potential of the photocatalyst was determined by microelectrophoresis (JS94H, PowerEach). The separation and transfer behaviors of photoelectrons was measured by photoluminescence spectroscopy (PL, F97Pro, Lengguang) and an electrochemical work-station (EIS, CHI660E, Chenhua). The work function was calculated based on density functional theory (DFT) with the plane-wave pseudopotential method. The cutoff energy was set to 450 eV; the energy convergence standard was 1×10^{-6} eV and the force convergence standard for each atom was −0.01 eV $Å^{-1}$.

2.4. Photocatalytic experiment

The photocatalytic performance of the photocatalyst was evaluated with MB and MO solution (20 mg L^{-1}) as the target degradation materials. The light source used in the photocatalytic test was a 300 W W-XE lamp with a UV cut-off filter

(λ > 420 nm) to provide the visible light spectrum. 0.1 g photocatalysts were put into 100 mL pollutant solution for dark adsorption for 60 min, and then the light source was used for degradation. 1 mL irradiated sample was collected every 5 min for photocatalytic evaluation. Also, the absorbance of the supernatant was measured by a UV-vis spectrophotometer (SP-752, Spectrum Instruments) to reflect the degradation efficiency of the photocatalyst.

3. Results and discussion

3.1. Crystallographic and morphological analyses

Fig. 2 shows that the XRD pattern was implemented to determine the phases of the as-prepared samples. Four formulations of composite photocatalysts with a mass fraction of Ag (0 wt%, 0.1 wt%, 0.5 wt%, 1 wt%) in the as-prepared samples were produced to optimize the degradation efficiency of the dye pollutants. The XRD results indicated that the triclinic phase $Ag_{10}Si_4O_{13}$ (JCPDS No. 71-1365) were obtained in all the samples, and the major peak (111) of the silver simple substance (JCPDS No. 14-0688) at about 38.1° were detected with the introduction of silver nitrate exceeding the silver–silicon molar ratio of $Ag_{10}Si_4O_{13}$. This indicates that the controlled *in situ* formation of the silver simple substance by adjusting the composition with molecular (ion) level of raw materials combined with sol–gel method and thermal reduction assistance.

The morphology and microstructure of GO, AG, and 0.5% AAG were characterized by TEM. Fig. 3(a) shows the gauzy GO with wrinkles prepared by improved Hummers' method. Fig. 3(b) is the TEM image of AG, the nanoparticles grow uniformly on GO, and the selected area electron diffraction (SAED) result confirmed the diffraction spots corresponding to the $(2\bar{1}3)$ and $(\bar{1}01)$ crystal planes of $Ag_{10}Si_4O_{13}$ (Fig. 3(c)). After the introduction of the silver simple substance, the composite material with uniformly dispersed growth of nanoparticles can still be obtained (Fig. 3(d) and (f), 0.5AAG). The direct contact between $Ag_{10}Si_4O_{13}$ and Ag (Fig. 3(f) and (g)) provides the possibility for the formation of the Schottky junction. The high-resolution (HR) TEM image shows the existence of the $(\bar{1}41)$ plane of $Ag_{10}Si_4O_{13}$ in alignment with a *d*-spacing of 0.197 nm and the (111) plane of Ag in alignment with a *d*-spacing of 0.235 nm (Fig. 3(g)). Meanwhile, the diffraction spots corresponding to the (020) plane of $Ag_{10}Si_4O_{13}$ and the (111) plane of Ag can be detected in the SAED data (Fig. 3(h)). The average sizes of the 0.5AAG nanoparticles are about 8.7 nm (Fig. 3(e)), which indicates that the utilization of GO as a carrier is helpful for the further grain refinement of $Ag_{10}Si_4O_{13}$.[26]

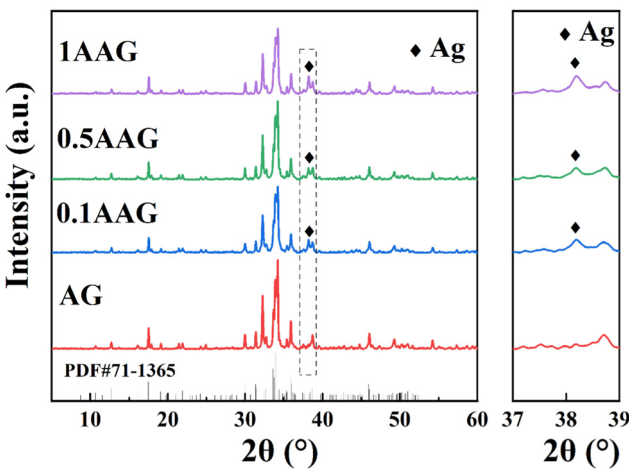

Fig. 2 XRD patterns of AG and AGG composites.

3.2. Chemical state and assembly mechanism of heterojunction analyses

FTIR was employed to analyze the functional group information. Fig. 4 shows the FTIR spectra of GO, AG, and 0.5AGG. In the FTIR spectrum of GO, the peaks of alkoxy/alkoxide C–O stretching (1050 cm^{-1}), carboxy C–O (1390 cm^{-1}), aromatic C=C (1640 cm^{-1}), and C=O (1730 cm^{-1}) were detected.[39] Also, the peaks at about 706 cm^{-1}, 1020 cm^{-1}, and 1380 cm^{-1} in AG and 0.5AGG did not change the position, which were assigned to the Si–O–Si bending vibration, Si–O stretching vibration, and Ag–O stretching vibration, respectively.[40] This indicates that the addition of Ag has no effect on the crystal structure of $Ag_{10}Si_4O_{13}$ in AGG. Due to the small dosage of GO, its characteristic peak was not detected in AG and 0.5AGG. However, a weak peak appeared at 1060 cm^{-1} in both AG and AGG, which may be attributed to the overlap of the peak of the Si–O–C bands with surrounding Si–O–Si bands,[41] which indicates that the complex assembly ultimately ensures the chemical bonding between GO and $Ag_{10}Si_4O_{13}$.

The surface composition and chemical state of elements of AG and 0.5AAG were studied by X-ray photoelectron spectroscopy (XPS), as shown in Fig. 5. The main peaks in the survey spectrum correspond to Ag 3d, Si 2p, O 1s, and C 1s orbitals (Fig. 5(a)). Fig. 5(b) shows the fitting spectra of Ag 3d orbitals; the peaks located at 368.0 (367.9) eV and 374.0 (373.9) eV were assigned to Ag^+ $3d_{5/2}$ and Ag^+ $3d_{3/2}$, and the peaks of 0.5 AGG located at 369.7 eV and 375.6 eV correspond to metallic Ag^0, respectively.[42,43] The peaks of Si $2p_{3/2}$ and Si $2p_{1/2}$ partially overlap with Ag 4s in $Ag_{10}Si_4O_{13}$ and the peaks located at 101.2 eV and 103.0 (103.2) eV correspond to Si $2p_{3/2}$ and Si $2p_{1/2}$, respectively (Fig. 5(c)).[44] The peaks of 530.0 eV and 532.2 (532.5) eV are the characteristic peaks of O 1s, corresponding to the Ag–O and Si–O bonds, respectively. For the C 1s orbital, the peak of 284.8 eV is the characteristic peak of surface correction carbon, and the characteristic peaks of the C–O bonds contained in GO were detected at 286.5 (286.6) eV.[39]

The binding energies of the above characteristic peaks of AG and 0.5AGG were all changed. Except for the decrease in the Ag^+ $3d_{5/2}$ and Ag^+ $3d_{3/2}$ binding energies of 0.5 AGG, the binding energy of Si $2p_{1/2}$, O 1s of Si–O, and C 1s of C–O were all increased. The increase in the binding energies of O 1s of Si–O and C 1s of C–O may be attributed to the formation of the Si–O-C bond.[41]

Based on the above analysis, a possible assembly mechanism of AGG can be proposed, as shown in Fig. 6.[45,46] The adoption of the sol gel method can realize the molecular (ion)-scale dispersion of the Ag-source, which lays a foundation for

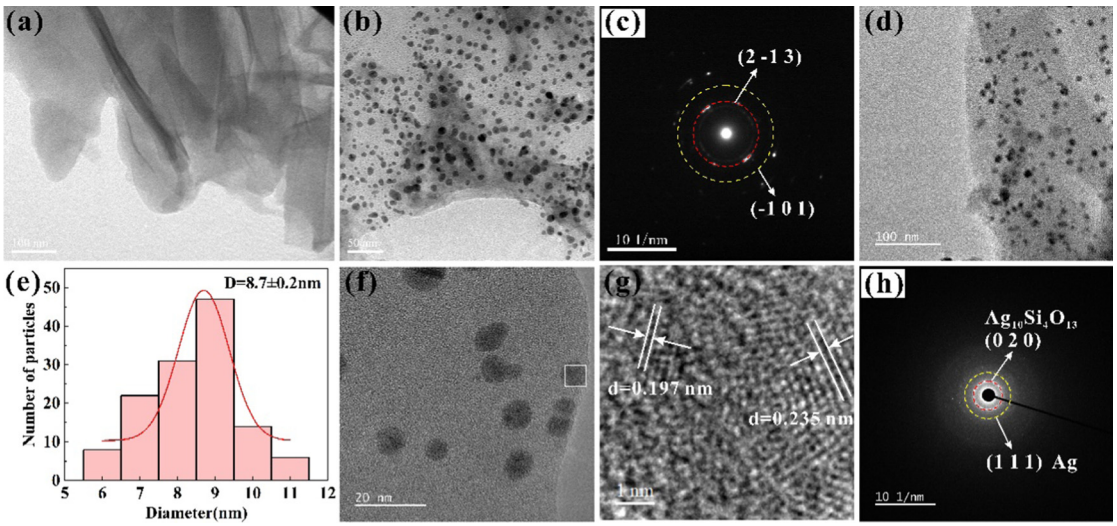

Fig. 3 TEM images of morphology and microstructure of GO and 0.5AGG. TEM image of GO (a). TEM image of AG (b). SAED image of AG (c). TEM image of 0.5AAG (d and f). Size distribution of Ag/$Ag_{10}Si_4O_{13}$ nanoparticles (e). HRTEM image of 0.5AAG (g). SAED image of AAG (h).

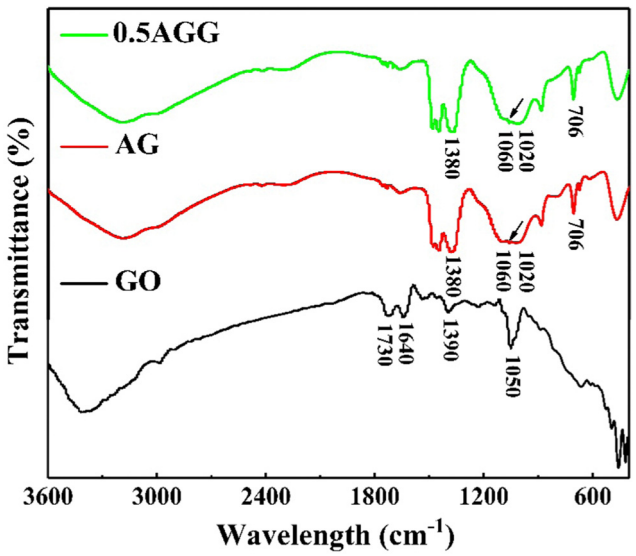

Fig. 4 FTIR spectra of GO, AG, and 0.5AAG composites.

the controllable assembly of the AAG composites and the controllable introduction of the silver simple substance. The citric acid molecules can coordinate with hydrolyzed products of TEOS. Further complexation will occur between the functional groups of TEOS or citric acid with GO. Then, the negative charges exposed due to the hydrolysis of remanent carboxyl will trap the silver ions with static electricity. Ultimately, the directional grafting of the complexes on the GO surface provides a more potent steric hindrance effect, resulting in a further refinement of the $Ag_{10}Si_4O_{13}$ grains.

3.3. Ultraviolet-visible and photoluminescence spectroscopy

The UV-vis diffuse reflectance results of the as-prepared samples with different dosages of silver are shown in Fig. 7(a). The absorption edge of AG is 610 nm. Also, the corresponding values of the AGG samples can reach about 660 nm, which undergo significant red-shifts. Moreover, the light absorption capacity was expanded throughout the 660 nm range. The energy bandgaps (E_g) of the as-prepared samples were calculated using magnified wavelength, corresponding to the Tauc plot.[47] According to the relationship between $(\alpha h\nu)^{1/2}$ and E_g in the inset of Fig. 7(a), the E_g of AG and 0.5AAG are 1.88 and 1.78 eV, respectively. When the frequency of incident illumination meets the resonance condition of silver nanoparticles, the LSPR is accompanied by absorption and scattering of light, which will induce light absorption occurs in the visible region.[48,49] Therefore, compared to AG, the absorption edge and the light absorption capacity of AGG were expanded.

Some photogenerated electrons and holes of the excited semiconductors will be combined and released in fluorescence if the spin-state is conserved. Therefore, innate fluorescence intensity reflects the recombination rate of the photogenerated electrons and holes. Fig. 7(b) shows the PL spectra of the as-prepared samples with different dosages of silver. The AGG samples exhibited lower fluorescence intensity compared to AG, and 0.5AGG shows the lowest fluorescence intensity. Due to the difference of WF of Ag, GO, and $Ag_{10}Si_4O_{13}$, the photoelectrons produced in the conduction band of $Ag_{10}Si_4O_{13}$ will inject into Ag or GO under the double action of the interface electric field of the heterojunction and the internal polarized electric field of $Ag_{10}Si_4O_{13}$. The Schottky junction will prevent photoelectron backflow to the barrier. As a result, a higher separation efficiency of photogenerated electrons and holes will be obtained by the AGGs. However, when the Ag dosage is much higher, the overlapping Ag nanoparticles can provide a good conductor of electrons and become their recombination center, which results in a higher recombination rate.

3.4. Electrochemical properties

Electrochemical properties were tested to further explore the generation, separation, and transfer mechanisms of the photoelectron. The flat band potentials obtained from the Mott–Schottky curve

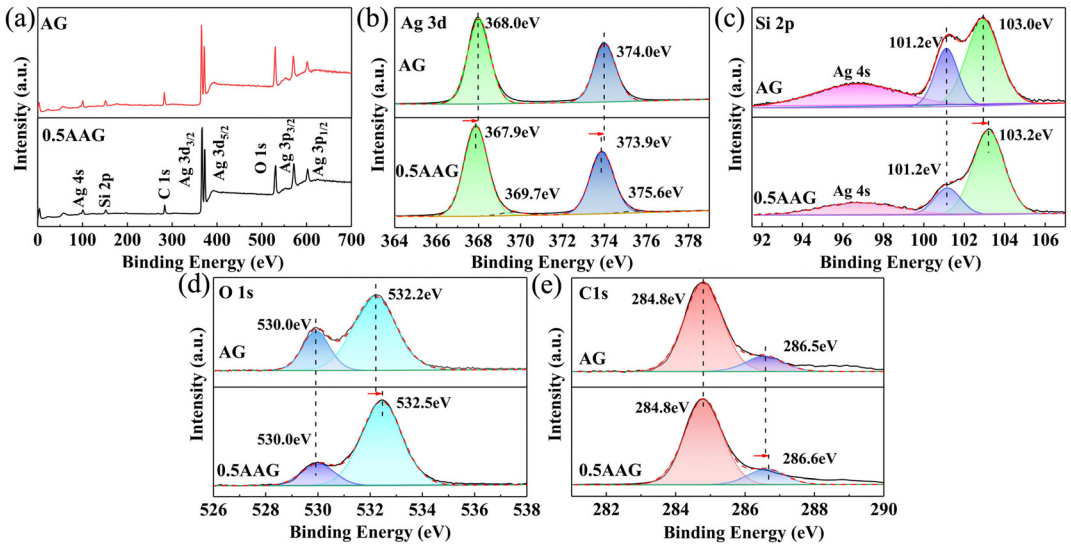

Fig. 5 The XPS survey spectra of AG and 0.5AAG (a), and high-resolution spectra of Ag 3d (b), Si 2p (c), O 1s (d), C 1s (e).

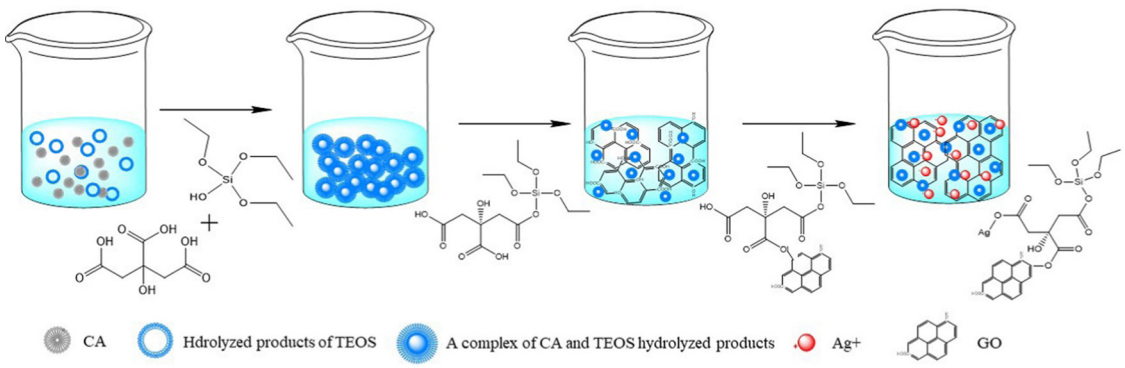

Fig. 6 The assembly mechanism of the AGG precursor.

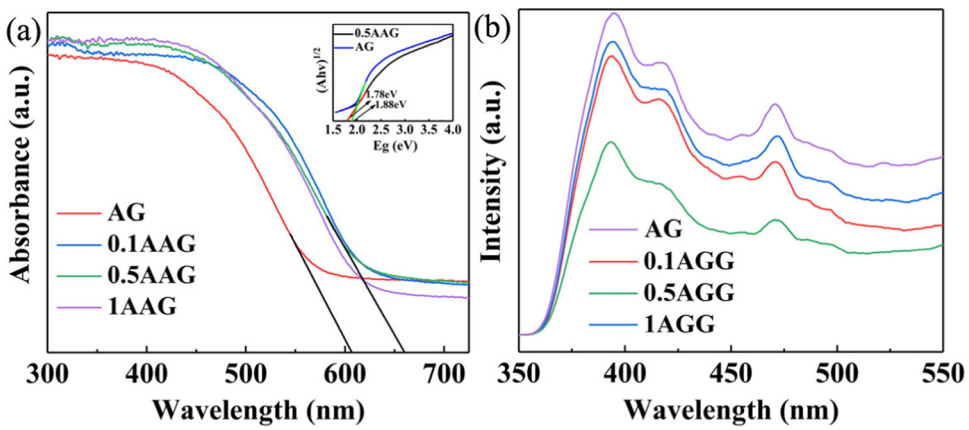

Fig. 7 The UV-vis DRS (a) and PL spectra (b) of AG and AAG composites.

infer the energy level structure, and then determine the positions of the valence band or conduction band of the semiconductors. Fig. 8(a) and (b) shows the Mott–Schottky curves of AG and 0.5AGG at 1000 Hz. The slopes of these curves are positive values, indicating that AG and 0.5AGG are all n-type semiconductors. Compared with the saturated calomel

electrode (SCE), the flat band potentials of AG and 0.5AGG are 0.37 eV and 0.31 eV, respectively, which possess flat band potentials of 0.61 eV and 0.55 eV relative to the standard hydrogen electrode (NHE). For the n-type semiconductor, its flat band potential is approximate to the conduction band.[50] Therefore, the valence band position of AG and 0.5AGG can be calculated as 2.49 eV and 2.33 eV according to the formula $E_{CB} = E_{VB} - E_g$, which was close to the valence band spectra of 2.56 eV and 2.41 eV obtained by XPS (Fig. 8(c)). Compared with AG, not only the narrower E_g of 0.5AGG contributes to the charge separation, its valence band is still in a position with strong oxidation ability (Fig. 8(d)).

The EIS measurement was employed to determine the charge transfer capability of the photocatalysts, as shown in Fig. 8(e). The Nyquist arc radius determines the resistance value of the photocatalyst.[51] The radii of AGGs are all lower than AG and decrease with the increase in silver dosages. This indicates that the introduction of Ag effectively lowered the interface charge transfer resistance. The transient photocurrent response reflects the rapid generation, separation, and transfer of charge carriers under on and off conditions of illumination. The photocurrent intensities of the as-prepared samples exhibit consistent evolution law as PL (Fig. 8(f)). Under the synergistic action of LSPR and Schottky junction, the photoelectron separation ability of AGGs is greatly improved. Similarly, excess silver provides photoelectron recombination centers that reduces the strength of the photocurrent intensity.

3.5. Zeta potential and adsorption property

The capture of pollutants by adsorption contributes to the improvement of the degradation performance. Fig. 9(a) shows the zeta (ζ) potential of the as-prepared samples in suspended distilled water. Overall, the potentials of these photocatalysts are all negative, and the absolute potential of AGGs are all higher than that of AG. 0.5AGG has the relatively highest absolute value of potential, indicating that its particle surface can provide the most adsorption active sites. Confirmed by dark adsorption measurement, the adsorption performance of AGGs is better than that of AG. The difference in the adsorption performance between AGGs was small, and 0.5AGG showed the best performance, which was consistent with the potential test (Fig. 9(b)). The silver oxide layer produced by the oxidation of silver can react with H_2O molecules.[52] Although most of the Ag^+ ions ionize into water and contribute to the formation of the double-layer surrounding the particles, $Ag(OH)^{2-}$ can provide a highly hydrophilic surface of the photocatalyst. This provides more active sites for the adsorption of MB. However, excessive silver may lead to a relative reduction of the exposed interfaces due to the overlapping effect, resulting in a slight decrease in the adsorption performance.

3.6. Photocatalytic reactivity of dye degradation

Cationic dyes methylene blue (MB) and anionic dyes methyl orange (MO) were used to evaluate the photocatalytic performance of the as-prepared samples. For the adsorbed equilibrium MB solution, the AG sample can reach a degradation rate of 99% at 25 min under visible light and a significant performance improvement occurred in the AAG samples, as shown in Fig. 10(a). MB was completely degraded in 15 min by AGGs, which takes 40 percent less time than AG. According to the Langmuir-Hinshelwood dynamics model, the degradation process of MB by nano-$Ag_{10}Si_4O_{13}$ conforms to the pseudo-first-order kinetic model (Fig. 10(b)). The reaction constants of AGGs are 0.2330 min^{-1}, 0.2436 min^{-1}, and 0.2352 min^{-1}, respectively, which is much higher than the value of AG (0.0995 min^{-1}). Fig. 10(c) shows the UV-vis absorption spectrum of the MB degradation process, which inferred that the degradation occurs within 15 min exposure to visible light, confirming carbon bond fission of the heterocycle of MB. The degradation of MO by as-prepared samples was relatively slower

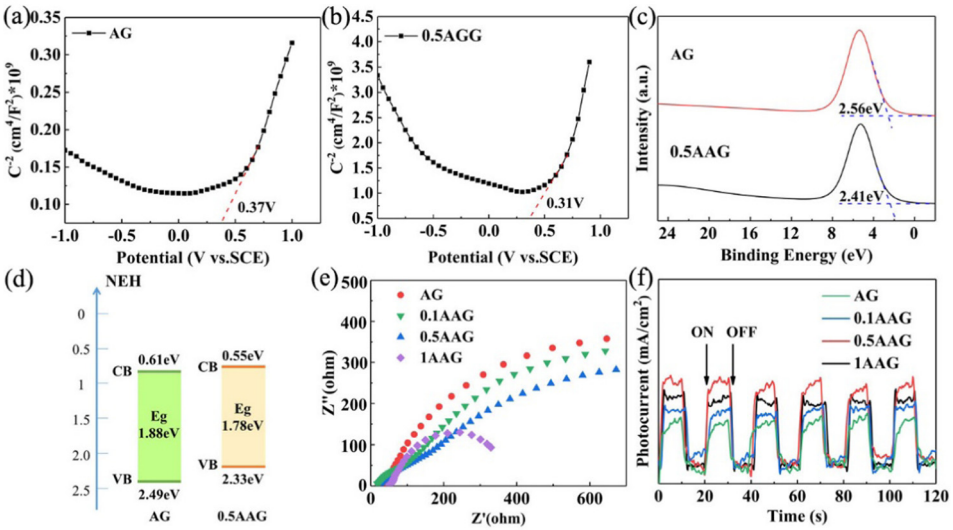

Fig. 8 Mott–Schottky plot of AG (a) and 0.5AAG (b) composites. The valence band spectra of AG and 0.5AAG composites (c). Bandgap position of AG and 0.5AAG composites (d). Nyquist plot of AG and AAG composites (e). Photocurrent response plot of AG and AAG composites (f).

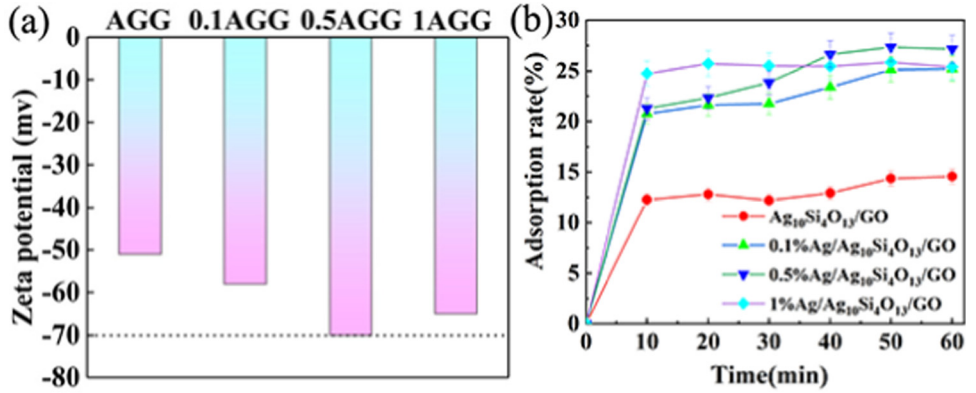

Fig. 9 The zeta potential in distilled water (a) and adsorption rate for MB of AG and AGG composites (b).

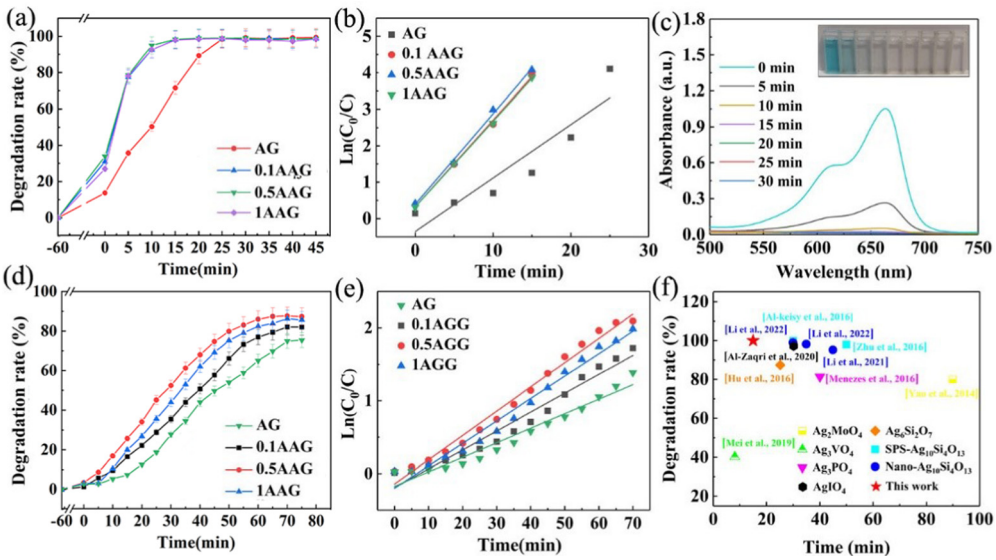

Fig. 10 The visible light degradation rate of AG and AGG composites for MB (a). The pseudo-first-order kinetic plots of AG and AGG composites for MB (b). The UV-vis absorption spectrum of the degradation process of 0.5AGG (c). The visible light degradation rate of AG and AGG composites for MO (d). The pseudo-first-order kinetic plots of AG and AGG composites for MO (e). A performance comparison of 0.5AAG with other Ag-based photocatalysts under visible light (f).

(Fig. 10(d) and (e)). The degradation rate of AG to MO at 70 min is 75%. The degradation rates of AGGs were improved, and 0.5AGG showed the most outstanding performance, with a degradation rate of 87% at 70 min.

For the positive MB molecules, the electrostatic adsorption by the as-prepared samples can capture its molecules to efficiently *in situ* degrade. As for MO molecules, the dark adsorption measurements confirmed that the photocatalysts showed no adsorption effect due to electrostatic repulsion. The degradation of MO mainly depends on the dynamic contact between its molecules with active substances on the photocatalyst interface; thus, the degradation efficiency is relatively lower. This indicates that AGG for the degradation of dyes is non-selective. Fig. 10(f) shows a performance comparison with other Ag-based photocatalysts under visible light. Compared to Ag_2MoO_4,[53] Ag_3VO_4,[54] Ag_3PO_3,[55] and $AgIO_4$,[56] the degradation rates based on 0.5AAG in this work have obvious advantages for MB. The performance of silver silicate ($Ag_6Si_2O_7$,[57] SPS-$Ag_{10}Si_4O_{13}$,[22,23] and nano-$Ag_{10}Si_4O_{13}$[3,26,27])-based photocatalysts is outstanding, but there is still a certain gap compared with that of AGG.

3.7. Degradation mechanism

The active radical capture experiments were carried out to evaluate the photocatalytic degradation mechanism of the photocatalyst (0.5AGG). The effects of electron (e^-), hole (h^+), superoxide radical ($^\bullet O_2$), and hydroxyl radical ($^\bullet OH$) on the photocatalytic performance are reported here. As shown in Fig. 11(a), the introduction of $AgNO_3$ as electron scavenger has no effect on the photocatalytic process, demonstrating that the electrons are hardly involved in the photocatalytic decomposition of dyes. The photocatalytic efficiency is significantly reduced by adopting TEOA and PTA chemical inhibitors, and the effect of TEOA is the most drastic. In addition, although the conduction band potential of 0.5AGG was far from reaching the

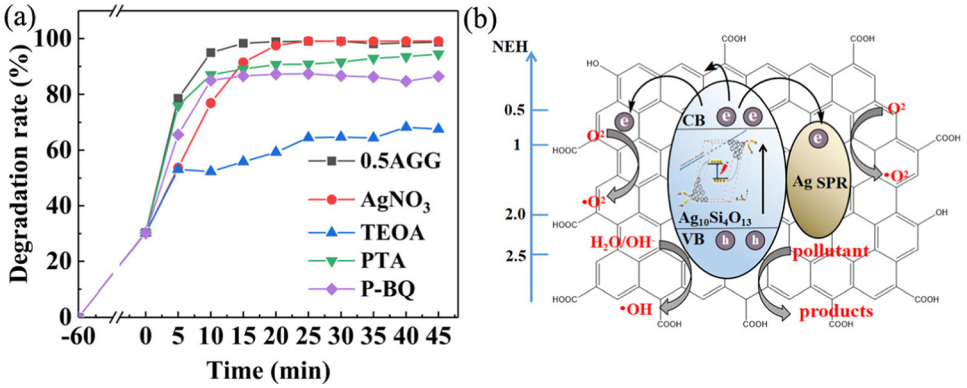

Fig. 11 Radical scavenging experiment (a) schematic diagram (b) of 0.5AAG.

formation position of $^{\bullet}O_2^-$ (−0.33 *vs.* NHE), the $^{\bullet}O_2^-$ exhibited a slight effect on the photocatalytic performance. This may be the result of interaction of photoelectrons transferred to GO and Ag nanoparticles with dissolved O_2 molecules on the surface.[58,59] This indicates that holes play a major role in the degradation of dyes by AGGs, and hydroxyl groups and superoxide free radicals also promote the degradation.

$Ag_{10}Si_4O_{13}$ is endowed with high visible light photocatalytic potential due to its inherent narrow bandgap and internal polarized electric field. On this basis, $Ag_{10}Si_4O_{13}$ with finer grains were obtained by use of GO as the carrier, the shorter pathway of electrons and holes transfer to the surface, and the more abundant reaction sites can ensure the carriers to participate in the photocatalytic reaction efficiently. With the introduction of silver nanoparticles, the synergistic effect of LSPR and Schottky junction can effectively prevent the backflow of hot electrons and photoelectron to silver nanoparticles and improve light utilization. The presence of GO can provide a pathway for electron transfer and contribute to more efficient separation of charge carriers, as shown in Fig. 11(b). In this way, the participation of holes in $Ag_{10}Si_4O_{13}$ and silver nanoparticles for the photodecomposition of dyes improved the photocatalytic performance significantly.

3.8. Cyclic service characteristic

Multiple cycle performance tests were used to evaluate the serviceability of photocatalysts. The results of cycle test performed five times are shown in Fig. 12(a) and (b). The photocatalytic performance of AG shows a decrease after the third cycle and decreased by 10% after the fifth cycle. The performance of 0.5AGG maintained an excellent stability; the degradation performance of the fifth cycle can still reach 98%. To further explore the evolution of performance stability, photocatalysts from each cycle test were collected and tested for XRD, as shown in Fig. 12(c) and (d). The peak intensities of the (111) plane of Ag all increased due to the photoreduction of Ag^+. According to the peak strength ratio of the (111) plane of $Ag_{10}Si_4O_{13}$ and the $(1\bar{3}2)$ plane of Ag, the contents of

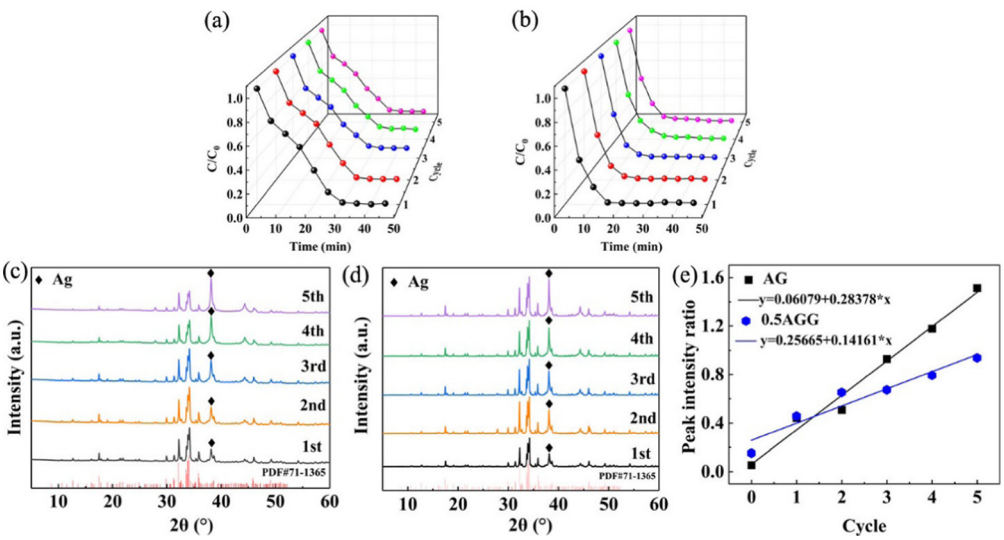

Fig. 12 The photocatalytic stability of AG (a) and 0.5AAG (b) composites. The XRD patterns of the AG (c) and 0.5AAG (d) composites after the degradation of MB. The peak intensity ratio of the $(1\bar{3}2)$ plane of $Ag_{10}Si_4O_{13}$ with the (111) plane of Ag (d). The contents of silver in AG and 0.5AGG increases with the number of cycles (e).

silver in AG and 0.5AGG increases with the number of cycles (Fig. 12(e)). For the 0.5AAG sample, Ag contents increase slowly after 3 cycles, indicating the effective protection of the Schottky junction on the stability of material composition and photocatalytic performance. As a whole, AGG has a considerable efficiency and stable service characteristic, which provides a new strategy to design and develop visible-light-driven photocatalysts.

4. Conclusion

In summary, a novel synthetic strategy for fabricating AAG nano-heterojunction was proposed by accurate molecular (ion) scale assembly based on the sol–gel method. The coordination between Ag-source, Si-source, and GO supported by CA molecules acted as chelated pendant, resulting in the *in situ* synthesis of nanostructured $Ag/Ag_{10}Si_4O_{13}$ Schottky junction uniformly loaded on the GO surface. The red-shifted edge of the absorption band of the AAG photocatalyst confirmed a prominent visible light response capacity. The outstanding charge separation efficiency was obtained due to the multiple function of LSPR, Schottky junction, and the internal polarization electric field of $Ag_{10}Si_4O_{13}$. The AAG photocatalyst was found to be highly efficient in the non-selective degradation of anionic and cationic dyes under visible light; the degradation efficiency of MB and MO (20 g mL^{-1}) can reach 100% (15 min) and 87% (70 min), respectively. Photodecomposition reactions were driven by photogenerated holes (h^+) assisted by $^{\bullet}OH$ and $^{\bullet}O_2^-$ radical species. An excellent cycle performance and compositional stability were confirmed by five cycles (reached 98% after the fifth cycle). The synthetic strategy provides a simple route for the design and fabrication of highly active visible light-responsive photocatalysts.

Conflicts of interest

There are no conflicts to declare.

Acknowledgements

This work was supported by the National Natural Science Foundation of China (No. 522020096), the Natural Science Foundation of Gansu Province, China (No. 22JR5RA284), Gansu Province Science and Technology Program Grant (No. 22JR5RA281).

References

1 Q. Ge and H. Liu, Tunable Amine-functionalized Silsesquioxane-based Hybrid Networks for Efficient Removal of Heavy Metal Ions and Selective Adsorption of Anionic Dyes, *Chem. Eng. J.*, 2021, **5790**, 131370, DOI: 10.1016/j.cej.2021.131370.

2 X. Zhao, X. Wang and T. Lou, Preparation of Fibrous Chitosan/Sodium Alginate Composite Foams for the Adsorption of Cationic and Anionic Dyes, *J. Hazard. Mater.*, 2021, **403**, 124054, DOI: 10.1016/j.jhazmat.2020.124054.

3 C. X. Li, H. Z. Sun, H. Z. Jin, W. S. Li, S. Bashir and J. L. Liu, Performance of Ferroelectric Visible Light Type II $Ag_{10}Si_4O_{13}/TiO_2$ Heterojunction Photocatalyst, *Catal. Today*, 2022, **400-401**, 146–158, DOI: 10.1016/j.cattod.2022.03.009.

4 L. Wang, D. W. Bahnemann, L. Bian, G. Dong, J. Zhao and C. Wang, Two-Dimensional Layered Zinc Silicate Nanosheets with Excellent Photocatalytic Performance for Organic Pollutant Degradation and CO_2 Conversion, *Angew. Chem., Int. Ed.*, 2019, **58**, 8103–8108, DOI: 10.1002/anie.201903027.

5 O. B. Oppong, F. Opoku and P. P. Govender, Tuning the Electronic and Structural Properties of Gd-TiO_2-GO Nanocomposites for Enhancing Photodegradation of IC Dye: The Role of Gd^{3+} Ion, *Appl. Catal., B*, 2019, **243**, 106–120, DOI: 10.1016/j.apcatb.2018.10.031.

6 H. W. Tian, M. Liu and W. T. Zheng, Constructing 2D Graphitic carbon nitride Nanosheets/Layered MoS_2/Graphene Ternary Nanojunction with Enhanced Photocatalytic Activity, *Appl. Catal., B*, 2018, **225**, 468–476, DOI: 10.1016/j.apcatb.2017.12.019.

7 W. Tang, J. Chen, Z. Yin, W. Sheng, F. Lin, H. Xu and S. Cao, Complete removal of phenolic contaminants from bismuth-modified TiO_2 single-crystal photocatalysts, *Chin. J. Catal.*, 2021, **42**, 347–355, DOI: 10.1016/S1872-2067(20)63668-3.

8 S. A. Ansari, M. M. Khan, M. O. Ansari, J. Lee and M. H. Cho, Biogenic Synthesis, Photocatalytic, and Photoelectrochemical Performance of Ag–ZnO Nanocomposite, *J. Phys. Chem. C*, 2013, **117**, 27023–27030, DOI: 10.1021/jp410063p.

9 L. Yang, Y. Liu, R. Y. Zhang, W. Li, P. Li, X. Wang and Y. Zhou, Enhanced visible-light photocatalytic performance of a monolithic tungsten oxide/graphene oxide aerogel for nitric oxide oxidation, *Chin. J. Catal.*, 2018, **39**, 646–653, DOI: 10.1016/S1872-2067(17)62974-7.

10 H. W. Tian, K. Shen, X. Y. Hu, L. Qiao and W. T. Zheng, N, S co-doped graphene quantum dots-graphene-TiO_2 nanotubes composite with enhanced photocatalytic activity, *J. Alloys Compd.*, 2017, **691**, 369–377, DOI: 10.1016/j.jallcom.2016.08.261.

11 W. J. Zhang, Y. X. Ma, X. H. Zhu, S. J. Liu, T. An, J. Y. Bao, X. Y. Hu and H. W. Tian, Fabrication of Ag decorated g-C_3N_4/$LaFeO_3$ Z-scheme heterojunction as highly efficient visible-light photocatalyst for degradation of methylene blue and tetracycline hydrochloride, *J. Alloys Compd.*, 2021, **864**, 158914, DOI: 10.1016/j.jallcom.2021.158914.

12 M. M. Liu, S. M. Ying, B. G. Chen, H. X. Guo and X. G. Huang, Ag@g-C_3N_4 Nanocomposite: an Efficient Catalyst Inducing the Reduction of 4-Nitrophenol Chin, *J. Struct. Chem.*, 2018, **40**(10), 1372–1378, DOI: 10.14102/j.cnki.0254-5861.2011-3178.

13 M. L. Tang, Y. H. Ao, C. Wang and P. F. Wang, Facile synthesis of dual Z-scheme g-C_3N_4/Ag_3PO_4/AgI composite photocatalysts with enhanced performance for the degradation of a typical neonicotinoid pesticide, *Appl. Catal., B*, 2020, **268**, 118395, DOI: 10.1016/j.apcatb.2019.118395.

14 Z. Li, H. Dong, Z. Wu, J. Shen, D. Xu, R. He, L. Wan and S. Zhang, Novel p-n type porous Ag_2O/Bi_5O_7I heterojunction for Uv-vis-NIR activated high efficient photocatalytic

degradation of bisphenol A: Photoelectric properties and degradation mechanism, *Appl. Surf. Sci.*, 2020, **529**, 147162, DOI: 10.1016/j.apsusc.2020.147162.

15 X. Zhang, B. Ren, X. Li, Y. Xu, B. Liu, P. Yu, Y. Sun and D. Mei, Efficiently enhanced visible-light photocatalytic activity by in situ deposition of Ag@AgBr on g-C_3N_4/Fe_3O_4 magnetic heterogeneous materials, *Sep. Purif. Technol.*, 2021, **254**, 117596, DOI: 10.1016/j.seppur.2020.117596.

16 M. L. Ren, Y. H. Ao, P. F. Wang and C. Wang, Construction of silver/graphitic-C_3N_4/bismuth tantalate Z-scheme photocatalyst with enhanced visible-light-driven performance for sulfamethoxazole degradation, *Chem. Eng. J.*, 2019, **378**, 122122, DOI: 10.1016/j.cej.2019.122122.

17 Y. Lee, J. Kang, S. Park, C. Lee, J. Moon and P. Alvarez, Photocatalytic degradation of neonicotinoid insecticides using sulfate-doped Ag_3PO_4 with enhanced visible light activity, *Chem. Eng. J.*, 2021, **402**, 126183, DOI: 10.1016/j.cej.2020.126183.

18 H. B. Chang, J. B. Liu, Z. Dong, D. D. Wang, Y. Xin, Z. L. Jiang and S. S. Tang, Enhancement of Photocatalytic Degradation of Polyvinyl Chloride Plastic with Fe_2O_3 Modified $AgNbO_3$ Photocatalyst under Visible-light Irradiation, *Chin. J. Struct. Chem.*, 2021, **40**(12), 1595–1603, DOI: 10.14102/j.cnki.0254-5861.2011-3217.

19 T. G. Kim, D. H. Yeon, T. Kim, J. Lee and S. J. Im, Silver silicates with three-dimensional d^{10}-d^{10} interactions as visible light active photocatalysts for water oxidation, *Appl. Phys. Lett.*, 2013, **103**, 043904, DOI: 10.1063/1.4816431.

20 X. L. Zhu, Z. Y. Wang, B. B. Huang, W. Wei, Y. Dai, X. Y. Zhang and X. Y. Qin, Synthesis of Ag_9 (SiO_4) $_2NO_3$ through a reactive flux method and its visible-light photocatalytic performances, *APL Mater.*, 2015, **3**, 104413, DOI: 10.1063/1.4928595.

21 Z. Lou, B. Huang, Z. Wang, X. Ma, R. Zhang, X. Zhang, X. Qin, Y. Dai and M.-H. Whangbo, $Ag_6Si_2O_7$: a Silicate Photocatalyst for the Visible Region, *Chem. Mater.*, 2014, **26**, 3873–3875, DOI: 10.1021/cm500657n.

22 A. Al-keisy, L. Ren, D. Cui, Z. Xu, X. Xu, X. Su, W. Hao, S. Dou and Y. Du, A ferroelectric photocatalyst $Ag_{10}Si_4O_13$ with visible-light photooxidation properties, *J. Mater. Chem. A*, 2016, **4**, 10992, DOI: 10.1039/C6TA03578G.

23 X. Zhu, P. Wang, B. Huang, X. Ma, X. Qin, X. Zhang and Y. Dai, Synthesis of novel visible light response $Ag_{10}Si_4O_{13}$ photocatalyst, *Appl. Catal., B*, 2016, **315**, 315–322, DOI: 10.1016/j.apcatb.2016.06.048.

24 G. Zhao, S. Yang, L. Jiang and H. Zhang, One-pot synthesis and improved photocatalytic performance of $Ag_{10}Si_4O_{13}$/N–CeO_2 composites, *J. Mater. Sci.: Mater. Electron.*, 2018, **29**, 2282–2290, DOI: 10.1007/s10854-017-8144-3.

25 M. Dorraji, M. Rasoulifard, Z. Aghamoradi, A. Sareshkeh, H. Daneshvar and F. Esfahani, The role of carbon-based nanosheets in enhancement of photocatalytic activity of $Ag_{10}Si_4O_{13}$, *J. Photochem. Photobiol., A*, 2020, **394**, 112486, DOI: 10.1016/j.jphotochem.2020.112486.

26 C. X. Li, Y. Y. Zhang, H. Z. Jin, W. C. Kang, W. H. Kong and W. S. Li, Fabrication and Visible-light Photocatalytic Properties of Nano-$Ag_{10}Si_4O_{13}$, *Ceram. Int.*, 2021, **47**, 32460–32465, DOI: 10.1016/j.ceramint.2021.08.082.

27 C. X. Li, W. H. Kong, H. Z. Jin, W. C. Kang and W. S. Li, Construction of 3D Sponge-like Hierarchical Pore $Ag_{10}Si_4O_{13}$ Microblock Photocatalyst with Enhanced Photocatalytic Activities, *Colloids Surf., A*, 2022, **633**, 127829, DOI: 10.1016/j.colsurfa.2021.127829.

28 C. Bie, H. Yu, B. Cheng, W. Ho, J. Fan and J. Yu, Design, Fabrication, and Mechanism of Nitrogen-Doped Graphene-Based Photocatalyst, *Adv. Mater.*, 2021, **33**, 2003521, DOI: 10.1002/adma.202003521.

29 P. Madhusudan, S. Wageh, A. A. Al-Ghamdi, J. Zhang, B. Cheng and Y. Yu, Graphene-$Zn_{0.5}Cd_{0.5}S$ nanocomposite with enhanced visible-light photocatalytic CO_2 reduction activity, *Appl. Surf. Sci.*, 2020, **506**, 144683, DOI: 10.1016/j.apsusc.2019.144683.

30 G. C. Xie, K. Zhang, B. D. Guo, Q. Liu, L. Fang and J. R. Gong, Graphene-based materials for hydrogen generation from light-driven water splitting, *Adv. Mater.*, 2013, **25**, 3820–3839, DOI: 10.1002/adma.201301207.

31 X. Li, J. Yu, S. Wageh, A. A. Ghamdi and J. Xie, Graphene in photocatalysis: A review, *Small*, 2016, **12**, 6640–6696, DOI: 10.1002/smll.201600382.

32 B. F. Machado and P. Serp, Graphene-based materials for catalysis, *Catal. Sci. Technol.*, 2012, **2**, 54–75, DOI: 10.1039/C1CY00361E.

33 C. X. Li, H. Z. Sun, H. Z. Jin, X. Shi, W. S. Li and W. H. Kong, Construction and Photocatalytic Performance of 3D Hierarchical Pore rGO/TiO_2 Composites, *J. Inorg. Mater.*, 2021, **36**, 1039–1046, DOI: 10.15541/jim20200682.

34 B. Luo, D. Xu, D. Li, G. Wu, M. Wu, W. Shi and M. Chen, Fabrication of a Ag/Bi_3TaO_7 Plasmonic Photocatalyst with Enhanced Photocatalytic Activity for Degradation of Tetracycline, *ACS Appl. Mater. Interfaces*, 2015, **7**, 17061–17069, DOI: 10.1021/acsami.5b03535.

35 W. B. Hou and S. B. Cronin, A Review of Surface Plasmon Resonance-Enhanced Photocatalysis, *Adv. Funct. Mater.*, 2012, **23**, 1612–1619, DOI: 10.1002/adfm.201202148.

36 S. Xun, Z. Zhang, T. Wang, H. Li and D. Jiang, Synthesis of novel metal nanoparitcles/$SnNb_2O_6$ nanosheets plasmonic nanocomposite photocatalysts with enhanced visible-light photocatalytic activity and mechanism insight, *J. Alloys Compd.*, 2016, **685**, 647–655, DOI: 10.1016/j.jallcom.2016.05.260.

37 X. Feng, Z. Yu, Y. Sun, R. Long, M. Shan, X. Li, Y. Liu and J. Liu, Review MXenes as a new type of nanomaterial for environmental applications in the photocatalytic degradation of water pollutants, *Ceram. Int.*, 2021, **47**, 7321–7343, DOI: 10.1016/j.ceramint.2020.11.151.

38 C. X. Li, R. B. Hu, X. F. Lu, S. Bashir and J. L. Liu, Efficiency enhancement of photocatalytic degradation of tetracycline using reduced graphene oxide coordinated titania nanoplatelet, *Catal. Today*, 2020, **350**, 171–183, DOI: 10.1016/j.cattod.2019.06.038.

39 T. T. Tung, T. Y. Kim, J. P. Shim, W. S. Yang, H. Kim and K. S. Suh, Poly(ionic liquid)-stabilized graphene sheets and

their hybrid with poly (3,4-ethylenedioxy- thiophene), *Org. Electron.*, 2011, **12**, 2215–2224, DOI: **10.1016/j.orgel.2011.09.012**.

40 S. Jin, H. Zhao, N. Xu, H. Zheng and T. Xu, Z-scheme mpg-C_3N_4/$Ag_6Si_2O_7$ Heterojunction for Highly Efficient Photocatalytic Degradation of Organic Pollutants under Visible Light, *J. Alloys Compd.*, 2019, **803**, 834–843, DOI: **10.1016/j.jallcom.2019.06.350**.

41 A. V. Vasin, A. V. Rusavsky, D. V. Kysil, S. Prucnal, Y. P. Piryatinsky, S. P. Starik, I. Nasieka, V. V. Strelchuk, V. S. Lysenko and A. N. Nazarov, The effect of deposition processing on structural and luminescent properties of a-SiOC:H thin films fabricated by RF-magnetron sputtering, *J. Lumin.*, 2017, **191**, 102–106, DOI: **10.1016/j.jlumin.2016.10.029**.

42 Y. Yang, W. Guo, Y. Guo, Y. Zhao, X. Yuan and Y. Guo, Fabrication of Z-scheme plasmonic photocatalyst Ag@AgBr/g-C_3N_4 with enhanced visible-light photocatalytic activity, *J. Hazard. Mater.*, 2014, **271**, 150–159, DOI: **10.1016/j.jhazmat.2014.02.023**.

43 S. Song, B. Cheng, N. Wu, A. Meng, S. Cao and J. Yu, Structure effect of graphene on the photocatalytic performance of plasmonic Ag/Ag_2CO_3-rGO for photocatalytic elimination of pollutants, *Appl. Catal., B*, 2016, **181**, 71–78, DOI: **10.1016/j.apcatb.2015.07.034**.

44 J. Liu, W. Wei, Q. Tian, Z. Dai, Z. Wu, X. Xiao and C. Jiang, Anchoring of $Ag_6Si_2O_7$ nanoparticles on α-Fe_2O_3 short nanotubes as a Z-scheme photocatalyst for improving their photocatalytic performances, *Dalton Trans.*, 2016, **45**, 12745–12755, DOI: **10.1039/C6DT02499H**.

45 D. D. Mahdieh, H. Hoda and S. Y. Jamileh, Synthesis and improved photoactivity of magnetic quaternary nanocomposites consisting of Fe_3O_4@ZnO core@shell nanoparticles decorated ongraphene-oxide grafted poly-citric acid, *Phys. B*, 2019, **553**, 11–17, DOI: **10.1016/j.physb.2018.10.020**.

46 H. Xu, Y. Wang, R. Chen, Y. Bai, T. Li, H. Jin, J. Wang and H. Xia, A green-synthetic spiderweb-like Si@Graphene-oxide anode material with multifunctional citric acid binder for high energy-density Li-ion batteries, *Carbon*, 2020, **157**, 330–339, DOI: **10.1016/j.carbon.2019.10.046**.

47 B. Tian, Z. Shao, Y. Ma, J. Zhang and F. Chen, Improving the visible light photocatalytic activity of mesoporous TiO_2 via the synergetic effects of B doping and Ag loading, *J. Phys. Chem. Solids*, 2011, **72**(11), 1290–1295, DOI: **10.1016/j.jpcs.2011.07.024**.

48 S. S. Patil, Dk. R. Patil, S. K. Apte, M. V. Kulkarni, J. D. Ambekar, C. Park, S. W. Gosavi, S. S. Kolekar and B. B. Kale, Confinement of Ag_3PO_4 nanoparticles supported by surface plasmon resonance of Ag in glass: Efficient nanoscale photocatalyst for solar H_2 production from waste H_2S, *Appl. Catal., B*, 2016, **196**, 75–84, DOI: **10.1016/j.apcatb.2016.02.068**.

49 D. Wang, Y. Li, G. L. Puma, C. Wang, P. Wang, W. Zhang and Q. Wang, Ag/AgCl@helical chiral TiO_2 nanofibers as a visible-light driven plasmon photocatalyst, *Chem. Commun.*, 2013, **49**, 10367–10369, DOI: **10.1039/C3CC45193C**.

50 W. Wang, P. Xu, M. Chen, G. Zeng, C. Zhang, C. Zhou, Y. Yang, D. Huang, C. Lai, M. Cheng, L. Hu, W. Xiong, H. Guo and M. Zhou, Alkali Metal Assisted Synthesis of Graphite Carbon Nitride with Tunable Band-Gap for Enhanced Visible-Light-Driven Photocatalytic Performance, *ACS Sustainable Chem. Eng.*, 2018, **6**, 15503–15516, DOI: **10.1021/acssuschemeng.8b03965**.

51 B. N. Rashmi, S. F. Harlapur, B. Avinash, C. R. Ravikumar, H. P. Nagaswarupa, M. A. Kumar and M. S. Santosh, Facile green synthesis of silver oxide nanoparticles and their electrochemical, photocatalytic, and biological studies, *Inorg. Chem. Commun.*, 2020, **111**, 107580, DOI: **10.1016/j.inoche.2019.107580**.

52 G. Merga, R. Wilson, G. Lynn, B. H. Milosavljevic and D. Meisel, Redox Catalysis on "Naked" Silver Nanoparticles, *J. Phys. Chem. C*, 2007, **111**, 12220–12226, DOI: **10.1021/jp074257w**.

53 S. Yao, Z. Zheng, S. Chen and Z. Shi, Preparation, Characterization, Photocatalytic Activity of S and Ag co-Doped Mesoporous Titania Photocatalysts, *Chin. J. Chem. Phys.*, 2014, **27**, 732–738, DOI: **10.1063/1674-0068/27/06/732-738**.

54 F. Mei, K. Dai, J. Zhang, W. Li and C. Liang, Construction of Ag SPR-promoted step-scheme porous g-C_3N_4/Ag_3VO_4 heterojunction for improving photocatalytic activity, *Appl. Surf. Sci.*, 2019, **488**, 151–160, DOI: **10.1016/j.apsusc.2019.05.257**.

55 P. Menezes, A. Indra, M. Schwarze, F. Schuster and M. Driess, Morphology-Dependent Activities of Silver Phosphates: Visible-Light Water Oxidation and Dye Degradation, *ChemPlusChem*, 2016, **81**, 1068–1074, DOI: **10.1002/cplu.201500538**.

56 N. Al-Zaqri, A. Alsalme, M. A. Ahmed and A. H. Galal, Construction of novel direct Z-scheme $AgIO_4$- g-C_3N_4 heterojunction for photocatalytic hydrogen production and photodegradation of fluorescein dye, *Diamond Relat. Mater.*, 2020, **109**, 108071, DOI: **10.1016/j.diamond.2020.108071**.

57 Y. Hu, H. Zhong, T. Xu, N. Xu and H. Ma, Highly efficient $Ag_6Si_2O_7$/WO_3 photocatalyst based on heterojunction with enhanced visible light photocatalytic activities, *RSC Adv.*, 2016, **6**, 103289, DOI: **10.1039/C6RA23591C**.

58 X. Yang, J. Qin, Y. Jiang, K. Chen, X. Yan, D. Zhang, R. Li and H. Tang, Fabrication of P25/Ag_3PO_4/graphene oxide heterostructures for enhanced solar photocatalytic degradation of organic pollutants and bacteria, *Appl. Catal., B*, 2015, **166–167**, 231–240, DOI: **10.1016/j.apcatb.2014.11.028**.

59 R. Liu, W. Yang, G. He, W. Zheng, M. Li, W. Tao and M. Tian, Ag-Modified g-C_3N_4 Prepared by a One-Step Calcination Method for Enhanced Catalytic Efficiency and Stability, *ACS Omega*, 2020, **5**, 19615–19624, DOI: **10.1021/acsomega.0c02161**.